



Two-phase deformation of lower mantle mineral analogs



P. Kaercher^{a,*}, L. Miyagi^b, W. Kanitpanyacharoen^c, E. Zepeda-Alarcon^d, Y. Wang^e,
D. Parkinson^f, R.A. Lebensohn^g, F. De Carlo^e, H.R. Wenk^d

^a Department of Earth, Ocean and Ecological Sciences, University of Liverpool, Liverpool, UK

^b Department of Geology and Geophysics, University of Utah, Salt Lake City, UT, USA

^c Department of Geology, Chulalongkorn University, Bangkok, Thailand

^d Department of Earth and Planetary Science, University of California, Berkeley, CA, USA

^e Advanced Photon Source, Argonne National Laboratory, Lemont, IL, USA

^f Advanced Light Source, Lawrence Berkeley National Laboratory, Berkeley, CA, USA

^g Material Science and Technology Division, Los Alamos National Laboratory, Los Alamos, NM, USA

ARTICLE INFO

Article history:

Received 30 April 2016

Received in revised form 16 September 2016

Accepted 19 September 2016

Available online 17 October 2016

Editor: J. Brodholt

Keywords:

crystallographic preferred orientation
seismic anisotropy
two-phase deformation
lower mantle rheology
3D X-ray microtomography

ABSTRACT

The lower mantle is estimated to be composed of mostly bridgmanite and a smaller percentage of ferropericlase, yet very little information exists for two-phase deformation of these minerals. To better understand the rheology and active deformation mechanisms of these lower mantle minerals, especially dislocation slip and the development of crystallographic preferred orientation (CPO), we deformed mineral analogs neighborite (NaMgF₃, iso-structural with bridgmanite) and halite (NaCl, iso-structural with ferropericlase) together in the deformation-DIA at the Advanced Photon Source up to 51% axial shortening. Development of CPO was recorded *in situ* with X-ray diffraction, and information on microstructural evolution was collected using X-ray microtomography. Results show that when present in as little as 15% volume, the weak phase (NaCl) controls the deformation. Compared to single phase NaMgF₃ samples, samples with just 15% volume NaCl show a reduction of CPO in NaMgF₃ and weakening of the aggregate. Microtomography shows both NaMgF₃ and NaCl form highly interconnected networks of grains. Polycrystal plasticity simulations were carried out to gain insight into slip activity, CPO evolution, and strain and stress partitioning between phases for different synthetic two-phase microstructures. The results suggest that ferropericlase may control deformation in the lower mantle and reduce CPO in bridgmanite, which implies a less viscous lower mantle and helps to explain why the lower mantle is fairly isotropic.

© 2016 Published by Elsevier B.V.

1. Introduction

Geodynamic models predict large strains due to convection in the lower mantle (e.g. McNamara et al., 2002), which is composed primarily of ~70% volume (Mg, Fe)SiO₃ bridgmanite and ~25% volume (Mg, Fe)O ferropericlase with a few percent of CaSiO₃ perovskite and some Al-rich and silica phases. Understanding how these minerals deform under large strains is important for constraining mantle rheology and for explaining seismic observations. Because the bulk of the lower mantle is seismically isotropic (French and Romanowicz, 2014), diffusion creep, which typically does not promote crystallographic preferred orientation (CPO) and thus seismic anisotropy, has long been assumed to be the dom-

inant deformation regime in the lower mantle (e.g. Karato et al., 1995). However, recent deformation experiments of ferropericlase and bridgmanite aggregates find they do deform by dislocation creep at lower mantle pressures and temperatures (Girard et al., 2016). Polycrystal plasticity models suggest strong CPO will develop if the large strains in the lower mantle are accommodated by dislocation slip (Wenk et al., 2011). However, these models ignore the interaction of bridgmanite with weaker ferropericlase.

Ferropericlase is likely weaker than bridgmanite in the lower mantle (e.g. Amodeo et al., 2012; Kraych et al., 2016; Merkel et al., 2003). For deformation in a two-phase system with large strength contrast, microstructure greatly influences rheology (e.g. Handy, 1994). For example, if the weaker ferropericlase is not interconnected, then rheology of the lower mantle will mostly depend on bridgmanite, but if ferropericlase is interconnected, then it will

* Corresponding author.

E-mail address: kaercher@liverpool.ac.uk (P. Kaercher).

likely control deformation. Ferropericlasite may not only influence the development of crystallographic preferred orientation and seismic anisotropy more than previously thought (e.g. Cottaar et al., 2014), but mantle mixing (Girard et al., 2016), viscosity (Yamazaki and Karato, 2001) and slab stagnation (Marquardt and Miyagi, 2015) as well.

The role of ferropericlasite in lower mantle rheology is controversial. Resistivity measurements of bridgmanite–ferropericlasite aggregates grown at 25 GPa from ringwoodite found ferropericlasite to be interconnected at 1300–1700 K and thereby likely to control the bulk deformation (e.g. Yamazaki et al., 2014). Aggregates of various proportions of MgO and MgAl₂O₄-spinel were deformed in the D-DIA at 5 GPa and 800–1000 °C, with MgO accommodating the majority of strain and greatly weakening the aggregate at 25% volume (Li et al., 2007). In a recent study Girard et al. (2016) deformed ~70% bridgmanite + ~30% ferropericlasite aggregates with isolated ferropericlasite grains inside of a bridgmanite matrix in a rotational Drickamer apparatus up to 100% shear strain. They suggest ferropericlasite controlled deformation based on observations of strain weakening, large strength contrast between the two phases, and strain partitioning into ferropericlasite, even though it was not interconnected. In contrast, other studies find that if weaker ferropericlasite is present in ~25% volume, bridgmanite controls deformation. For example finite element modeling (FEM) of deformation in bridgmanite–ferropericlasite aggregates by Madi et al. (2005) found bridgmanite limits deformation even when both phases are highly interconnected. Wang et al. (2013) deformed 72% CaGeO₃-perovskite + 28% MgO with MgO as isolated grains in the microstructure in the D-DIA up to 20% axial shortening and found that the bridgmanite analog (CaGeO₃) controlled deformation.

Very few studies consider CPO (i.e. texture) development during deformation of lower mantle polymineralic aggregates. Of the studies mentioned above, only Wang et al. (2013) looked at CPO and found CaGeO₃ developed similar CPO whether deformed as a single phase or along with 28% volume MgO while MgO developed weak CPO. Wenk et al. (2004) and Miyagi and Wenk (2016) deformed ferropericlasite–bridgmanite aggregates to 50 GPa and 61 GPa, respectively, in a diamond anvil cell (DAC) and found that ferropericlasite developed a weak, irregular texture when deformed with bridgmanite, and that bridgmanite texture changed depending on the starting material and/or the presence of ferropericlasite. Microstructures in the DAC experiments were unknown but assumed to have ferropericlasite not interconnected based on earlier studies (e.g. Martinez et al., 1997), and thus attributed the lack of CPO in ferropericlasite to local heterogeneous deformation.

None of these studies considered the effect of ferropericlasite volume percent on CPO even though volume percent of ferropericlasite in the lower mantle is estimated from geophysical and geochemical data to be anywhere from 10 to 30% (Irifune and Tsuchiya, 2007) and is likely heterogeneously distributed in the lower mantle. Here we deformed two-phase lower mantle mineral analogs with various volume percent of each phase in the D-DIA at high temperature and pressure. Because the D-DIA cannot reach lower mantle pressures, we used analogs NaCl and NaMgF₃, isostructural to ferropericlasite and bridgmanite, respectively. X-ray diffraction images were collected *in situ* to observe the development of CPO and stress distribution in the two phases. We examined three-dimensional (3D) microstructures with X-ray microtomography and estimate slip systems responsible for the observed CPO and the effect of microstructure on stress and strain partitioning between phases with polycrystal plasticity models.

2. Materials and methods

2.1. Analog minerals

2.1.1. Neighborite

NaMgF₃ has a distorted cubic structure characterized by tilted MgF₆ octahedra and belongs to orthorhombic space group Pbnm. NaMgF₃ was chosen as an analog mineral for bridgmanite because it is isostructural to bridgmanite, yet deforms more easily at lower pressures. In addition, NaMgF₃ transitions to a CaIrO₃-type post-perovskite structure at high pressure, to tetragonal and cubic phases at high temperature, and dissociates at high pressures and temperatures just as bridgmanite does (e.g. Zhao et al., 1994; Umemoto et al., 2006; Umemoto and Wentzcovitch, 2011).

It is less clear whether NaMgF₃ has similar deformation mechanisms as bridgmanite. Twinning has been observed in both NaMgF₃ (e.g. Lewis and Bright, 1971) and in bridgmanite (e.g. Wang et al., 1990), and is commonly produced in perovskite structures, either during a phase transition or by deformation. Most deformation is accommodated by slip, however slip systems in NaMgF₃ have not been well studied, and the preferred slip systems of bridgmanite in the DAC suggest a number of slip systems on the (010), (001), and/or (100) planes (e.g. Merkel et al., 2003; Miyagi and Wenk, 2016), experiments in the multianvil apparatus suggest slip along ⟨100⟩ at uppermost lower mantle conditions (Cordier et al., 2004), and bonding calculations suggest (100)[010] slip at lower mantle conditions (e.g. Mainprice et al., 2008; Kraych et al., 2016). Deformation textures strongly show orthorhombic textures requiring orthorhombic rather than pseudo-cubic slip systems (Wenk et al., 2006), which is yet another reason for selecting NaMgF₃ with orthorhombic symmetry rather than a cubic perovskite as an analog. Results presented in section 4.2.1 show some similarity between CPO development and active slip systems in NaMgF₃ and bridgmanite.

NaMgF₃ was synthesized for this study from a stoichiometric mixture of NaF and MgF₂ sintered at 750 °C (see Appendix A).

2.1.2. Halite

NaCl was chosen as the analog for ferropericlasite, because it is isostructural to ferropericlasite. Both minerals have a B1 structure, belonging to space group Fm $\bar{3}$ m at ambient conditions. The deformation behavior of single crystal NaCl (e.g. Carter and Heard, 1970) and periclasite (e.g. Routbort, 1979; Day and Stokes, 1966) have been studied in detail. In both minerals, the stiffest direction is parallel to the *a*-axis, and the easiest slip system is {110}⟨1 $\bar{1}$ 0⟩, with {111}⟨1 $\bar{1}$ 0⟩ and {001}⟨1 $\bar{1}$ 0⟩ becoming increasingly active at higher temperature.

The strength contrast between bridgmanite and ferropericlasite (the ratio of maximum differential stress supported by each phase) at upper lower mantle conditions has been estimated to be about 5–10, depending on pressure and temperature (e.g. Amodeo et al., 2012; Kraych et al., 2016; Girard et al., 2016). Here we find the strength contrast between NaMgF₃ and NaCl at pressures near 4 GPa and temperatures 200–400 °C to be ~10. If the strength contrast is higher in the analog system, so too may be the degree of stress and strain partitioning and the degree of connectivity of the weaker NaCl (Handy, 1994).

2.2. Deformation-DIA

2.2.1. Experiments

Experiments were done in the D-DIA at GSECARS beamline 13-BM-D of the Advanced Photon Source (APS). The D-DIA is a multi-anvil press that can apply quasi-hydrostatic pressure up to

Table 1

Summary of run conditions and results from X-ray diffraction experiments. Volume percent of NaMgF₃ were before sintering (S) and from relative intensity of X-ray diffraction peaks during experiments (X). Standard strains (ϵ) are shown as percentages. The average steady state stress and maximum differential stress ($-\Delta\sigma$) and texture strength (pole density or "IPF max") are shown for each run. Since $-\Delta\sigma$ vs. ϵ does not plot steady state behavior for runs D1316 and D1315 (Fig. 2b), all stresses above 20% strain were averaged. Standard deviations for $-\Delta\sigma$ are <0.006 . The average total estimated stress for an interconnected weak layer (IWL) and a load bearing framework (LBF) have been calculated using equations (11) and (6), respectively, in Handy (1994).

Run	Experimental parameters					NaMgF ₃		$-\Delta\sigma$		NaCl		$-\Delta\sigma$		IWL	LBF
	V_{NaMgF_3}	P_{ave}	T_{mode}	ϵ	$\dot{\epsilon}$	IPF max		$-\Delta\sigma$		IPF max		$-\Delta\sigma$		$-\Delta\sigma$	$-\Delta\sigma$
	S/X (%)	(GPa)	(°C)	(%)	(s ⁻¹)	Ave. (mrd)	Max. (mrd)	Ave. (GPa)	Max. (GPa)	Ave. (mrd)	Max. (mrd)	Ave. (GPa)	Max. (GPa)	(GPa)	(GPa)
D1316	30/37	4.3	400	34	0.0027	3.0	3.6	0.30	0.67	1.3	1.4	0.07	0.17	0.11	0.16
D1243	30/33	4.5	200	44	0.0029	2.9	3.4	0.69	0.82	1.3	1.3	0.17	0.19	0.24	0.34
D1315	50/62	3.8	400	33	0.0023	3.3	3.4	0.34	0.89	1.1	1.2	0.06	0.15	0.10	0.23
D1244	50/59	4.0	200	50	0.0031	3.1	4.1	0.86	0.89	1.1	1.2	0.14	0.15	0.26	0.57
D1188	75/79	3.8	400	23	0.0022	4.0	4.2	1.19	1.24	1.1	1.2	0.10	0.12	0.30	0.96
D1187	75/80	4.8	100	32	0.0013	4.0	4.7	1.45	1.46	1.2	1.2	0.15	0.19	0.40	1.19
D1475	85/82	4.0	400	44	0.0023	4.6	5.4	1.24	1.35	1.3	1.5	0.17	0.19	0.38	1.05
D1476	85/85	4.3	200	51	0.0034	4.7	5.9	1.91	1.96	1.4	1.5	0.17	0.26	0.52	1.64
D1189	100	1.7 ^a	800	50	0.0027	5.9	6.9	0.74	1.05	-	-	-	-	-	-
D1185	100	3.7	400	32	0.0020	8.0	11.8	2.13	2.25	-	-	-	-	-	-

^a Pressure estimate is low because there is no thermal equation of state for NaMgF₃ that can take into account the high temperature in run D1189.

~15 GPa and uniaxial differential stress separately while simultaneously resistively heating up to 2000 °C (Wang et al., 2003).

Ten samples of various volume percent of NaMgF₃ and NaCl were compressed quasi-hydrostatically to 20 tons (~3–5 GPa) by driving in three sets of orthogonal pistons, then compressed uniaxially by advancing the differential rams (top and bottom pistons). Samples were deformed up to ~51% axial shortening at average strain rates of 1.3×10^{-3} to 3.4×10^{-3} s⁻¹ while being heated to temperatures ranging from 100 °C to 800 °C (Table 1). Diffraction images were collected in radial geometry (X-ray path is perpendicular to compression direction) with monochromatic X-rays ($\lambda = 0.225\text{--}0.248$ Å) as pressure and strain increased. During compression, axial shortening of the samples was imaged with X-ray radiography using two 5 μm thick flakes of Au on the top and bottom of the sample for contrast. Axial shortening is defined as standard strain % = $\Delta l/l_0 \times 100$ where l_0 is the sample length after quasi-hydrostatic compression but before deforming. In a few experimental runs where the rams did not advance at the same rate as the load, causing slight sample extension, l_0 is taken as the sample length at ambient pressure. Since compression in D-DIA is never truly hydrostatic, l_0 is likely measured at non-zero strain in all cases.

2.2.2. Data analysis

Diffraction images were analyzed with Rietveld refinement as implemented in the software package MAUD (e.g. Lutterotti et al., 2014). Rietveld refinement is a least-squares method that minimizes the difference between the data and a calculated fit by iteratively refining various parameters such as diffraction background, phase volume percent, cell parameters, crystallite size, root mean square (r.m.s.) microstrain, lattice strain, and CPO. Pressure was calculated from the best fit for cell parameters and equation of state of NaCl or NaMgF₃. Details of Rietveld refinement are given in Appendix B.

With Rietveld analysis we can quantify the differential stress and CPO in each phase. Deviatoric (non-hydrostatic) stress imposed on the sample leads to non-isotropic elastic lattice strain, which is exhibited as sinusoidal variations of diffraction peak position as a function of η (the angle to the compression direction, i.e. the azimuthal angle) (Fig. 1 and Fig. A.1). For each phase, the principle stresses in the deviatoric stress tensor (σ_{11} , σ_{22} , and σ_{33}) can be calculated from the non-isotropic lattice strain and the elastic constants of NaMgF₃ (Zhao and Weidner, 1993) and NaCl (Liu et al., 2010); see Appendix B for details. Differential stress is defined as $\Delta\sigma = \sigma_{33} - \sigma_{11}$, where σ_{33} is the principle stress in the direction of the loading axis, and σ_{11} and σ_{22} are the principal stresses per-

pendicular to the loading axis and are assumed to be equal. Here we define compressive stress to be negative and write $-\Delta\sigma$ to refer to compressive differential stress.

Plastic deformation by dislocation slip leads to rotation of crystallographic planes relative to a maximum stress direction and can result in CPO. The critical resolved shear stress (CRSS), i.e. the minimum stress required to activate slip in a set of crystallographic planes, of the possible slip systems will determine the resulting texture. CPO is exhibited as regular intensity variations in Debye rings along η (Fig. 1 and Fig. A.1). It is described by an orientation distribution function (ODF) and is plotted here as inverse pole figures (IPFs), which plot the density of poles of crystallographic planes relative to the compression direction of the sample.

2.3. Microtomography and microstructure

2.3.1. Microtomography experiments

Microtomography non-destructively images the 3D structure of samples using phase contrast imaging. Phase connectivity and distribution of one undeformed sample and three deformed samples were quantified using microtomography at beamline 8.3.2 of the Advanced Light Source (ALS) and beamline 2-BM of the APS.

Sample cylinder axes were positioned vertically on a mounting needle on a rotation stage using a small piece of clay. Either 1500 or 2049 transmission images were collected while the sample was rotated 180°. Transmission images were corrected for inhomogeneous illumination, normalized, and reconstructed into slices that were stacked to render a 3D image. Each phase was thresholded, and statistics were compiled in Avizo Fire 3D Analysis Software for Materials Science (Visualization Sciences Group). For more details of microtomography setup, collection, and analysis, see Appendix C.

2.3.2. Scanning electron microscopy

Since X-ray diffraction and microtomography could not resolve grain size in our samples, a backscattered image of an undeformed 75% NaMgF₃, unpolished sample was collected in a Zeiss Evo Ma10 environmental scanning electron microscope (ESEM) (Fig. 5b) at UC Berkeley to estimate grain size. The image was taken at 1000× magnification under elevated pressure so that the sample did not need to be carbon coated. The large difference in hardness between the two phases and the solubility of both phases in water, especially NaCl, makes these samples very challenging to prepare for electron backscatter diffraction (EBSD) requiring new polishing methods to be developed. In addition kikuchi patterns of orthorhombic perovskite minerals like NaMgF₃ that have two cell

parameters nearly equal in length are difficult to reliably index. Therefore we do not include further microstructural analysis of these samples here but plan to present EBSD and SEM results in a separate paper.

3. Results

Results are based on 120 X-ray diffraction images taken during ten experimental runs in the D-DIA. Errors of volume percent derived from X-ray diffraction patterns are roughly $\pm 0.2\%$ in most cases, but can be as high as $\pm 4\%$ (Table 1). These differ from percentages measured before sintering by more than 4%, which may be due to some powder being lost during the sintering process and/or the fact that the X-ray beam samples only a small section of the sample that might have slightly different composition.

3.1. Differential stress

A general trend of decreasing differential stress in NaMgF₃ with increasing NaCl content can be seen in Fig. 1 where the waviness (i.e. sinusoidal variation of peak positions along n) of NaMgF₃ peaks decreased with increasing NaCl content. The 100% NaMgF₃ sample deformed at lower temperature (400 °C) acquires the highest stress of $-\Delta\sigma_{\max} = 2.25$ GPa, which decreased to 1.35 GPa for 85% NaMgF₃, 1.24 GPa for 75% NaMgF₃, and <1 GPa for 50% NaMgF₃ and 30% NaMgF₃ samples (results for 400 °C runs, Table 1).

Increasing temperature reduced differential stress in NaMgF₃ and affected the 100% NaMgF₃ sample the most, with stress reaching up to $-\Delta\sigma_{\max} = 1.05$ GPa and averaging during steady state $-\Delta\sigma_{\text{ave}} = 0.74$ GPa at 800 °C, less than half of $-\Delta\sigma_{\max} = 2.25$ GPa and $-\Delta\sigma_{\text{ave}} = 2.13$ GPa at 400 °C (Table 1). The effect of temperature on $-\Delta\sigma$ in NaMgF₃ decreases with increasing NaCl content as shown in Fig. 2a, where $-\Delta\sigma_{\max}$ for runs done at higher temperature (half-filled markers) plot far below $-\Delta\sigma_{\max}$ for runs done at lower temperature (filled markers) in the 100% NaMgF₃ sample, but plot much nearer each other for the 75% NaMgF₃, 50% NaMgF₃, and 30% NaMgF₃ samples. The high temperature 100% NaMgF₃ run was done at 800 °C compared to 400 °C on average in high temperature runs for other samples (Table 1). This may explain why the data point for average differential stress for high temperature 100% NaMgF₃ falls below the best fit line in Fig. 2a.

Differential stress supported by NaMgF₃ increased until about 20% strain in 100% NaMgF₃ samples and until 10–15% strain in most two-phase samples, when steady state deformation was reached (Fig. 2b). The drop in differential stress for the low temperature run of 85% NaMgF₃ at about 40% strain and high temperature runs of 50% NaMgF₃ and 30% NaMgF₃ samples at about 33% strain in Fig. 2b is due to a temperature increase at the end of those experiments.

Because NaCl yields plastically at lower stress than NaMgF₃, it cannot support as much differential stress (lattice strain) before deforming plastically. This is seen in Fig. 1 where the NaCl peaks are relatively straight compared to NaMgF₃. Differential stress in NaCl reached up to $-\Delta\sigma_{\max} = 0.26$ GPa, nearly an order of magnitude less than NaMgF₃ at $-\Delta\sigma_{\max} = 2.25$ GPa (Table 1), giving an estimated strength contrast for NaMgF₃–NaCl of about 10. With such little stress development in NaCl, no strong correlation is seen between differential stress and bulk strain or sample composition (Fig. 2). Differential stress in NaCl slightly decreases at higher temperature (Fig. 2a) and very slightly peaks at 10% strain (Fig. 2b).

Using equations from Handy (1994), we estimate the total stress in the sample from the phase volume percent and the average steady state stress ($-\Delta\sigma_{\text{ave}}$) in each phase for both an interconnected weak layer (IWL) and a load bearing framework (LBF)

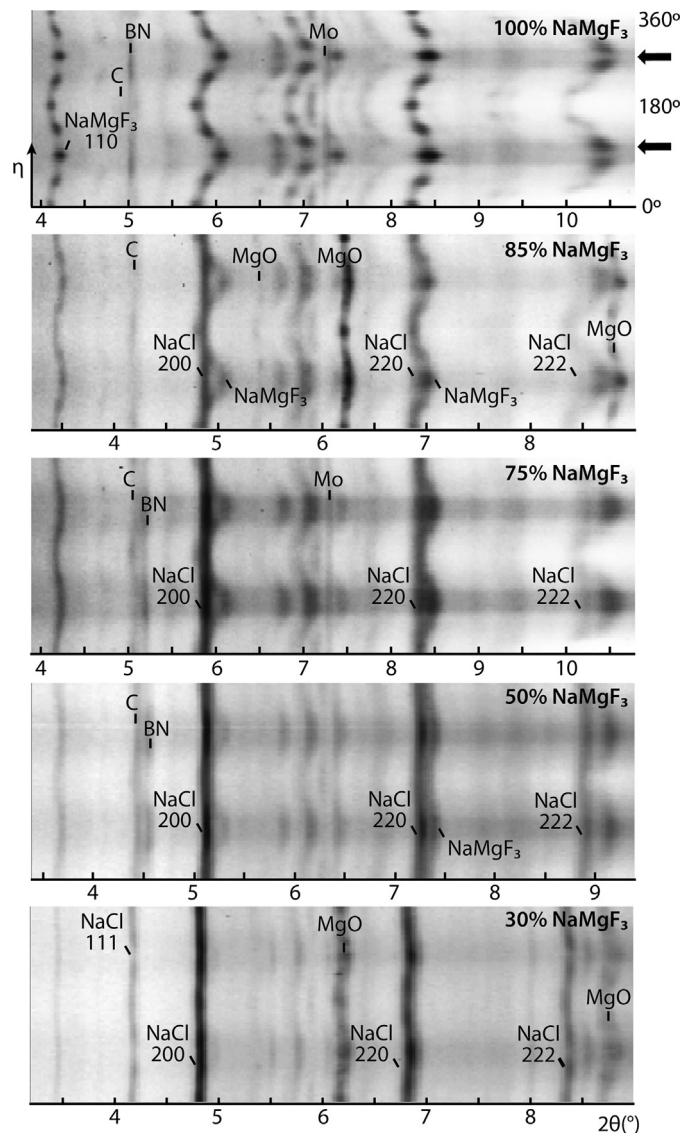


Fig. 1. Unrolled diffraction patterns for samples at 20 tons (~ 4 GPa), 100–400 °C, and 30% strain for all compositions. Peaks from the graphite heater (C), the insulation sleeve, either boron nitride (BN) or MgO, and small Mo contamination are labeled. The first NaMgF₃ peak, 110, is labeled. However, because diffraction from multiple NaMgF₃ planes contribute to each of the other peaks, these are not labeled. All unlabeled peaks are NaMgF₃. Compression direction is labeled with arrows in first image.

microstructure (Table 1). For samples with at least 50% volume NaCl, especially those deformed at higher average temperatures, the total $-\Delta\sigma$ estimated for an IWL ($-\Delta\sigma_{\text{IWL}}$) agrees much better with the average $-\Delta\sigma$ supported by NaCl than the total $-\Delta\sigma$ estimated for a LBF ($-\Delta\sigma_{\text{LBF}}$) agrees with $-\Delta\sigma$ supported by NaMgF₃. This suggests that the microstructures in these samples are closer to an IWL microstructure, as expected. For samples with less than 50% NaCl, neither does $-\Delta\sigma_{\text{IWL}}$ agree well with the average $-\Delta\sigma$ supported by NaCl nor does $-\Delta\sigma_{\text{LBF}}$ agree well with $-\Delta\sigma$ supported by NaMgF₃. This implies that the microstructures with lower NaCl content fall somewhere between an IWL and a LBF.

3.2. Texture

NaMgF₃ developed a pole density maximum at (100) in the IPFs for all compositions (Fig. 3a), indicating that (100) lattice planes preferentially align perpendicular to the compression direc-

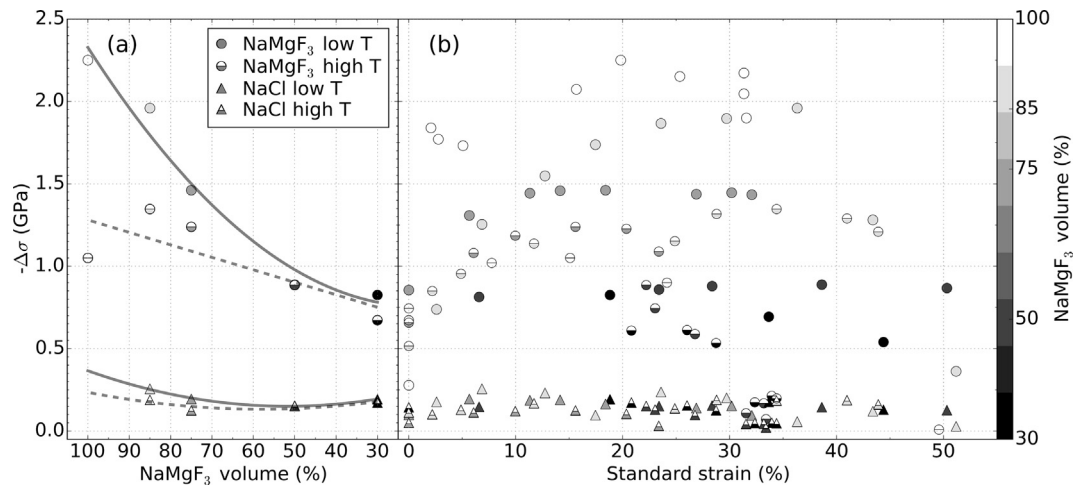


Fig. 2. (a) Scatter plot of maximum differential stress ($-\Delta\sigma$) versus composition in NaMgF₃ and NaCl for each run (see Table 1 for values). All compositions were deformed twice, once at higher average temperature (half-filled shapes) and once at lower average temperature (filled shapes). Best-fit curves are shown for average higher temperatures (dashed lines) and lower average temperatures (solid lines) for each phase. (b) Scatter plot of $-\Delta\sigma$ versus standard strain in NaMgF₃ and NaCl for ten experimental runs. Composition indicated by gray scale. All data shown was collected at 20 tons during sample compression.

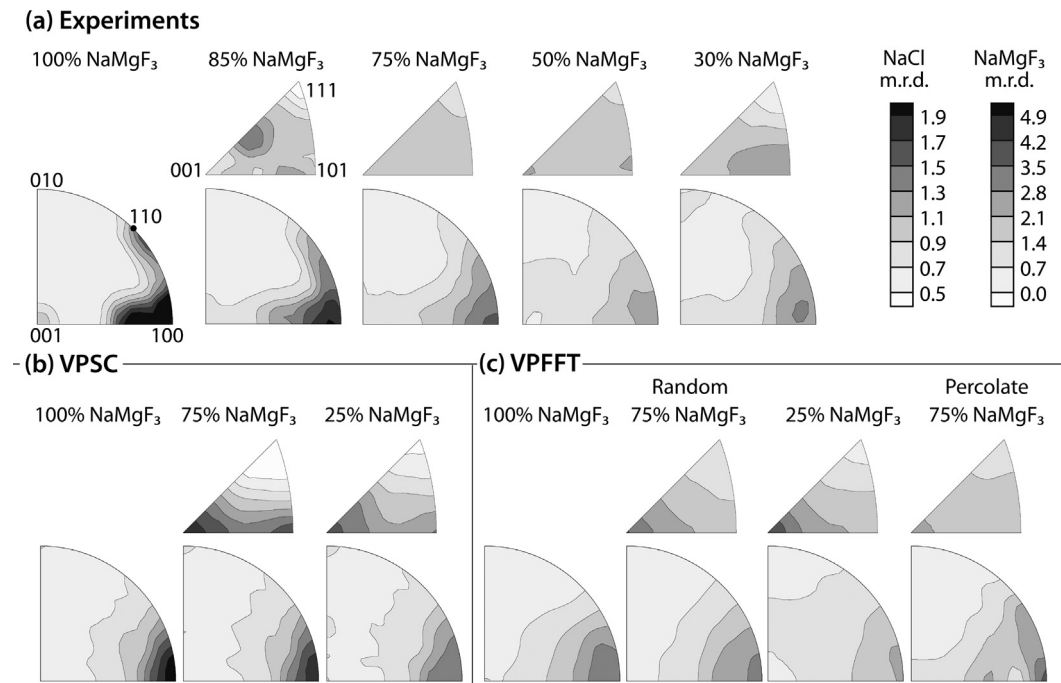


Fig. 3. Inverse pole figures (IPFs) from (a) experiments, which correspond to 2D plots shown in Fig. 2, collected at ~ 4 GPa, 100–400 °C, and $\sim 30\%$ strain, (b) VPSC simulations with relative CRSS assigned as shown in Table 3 to 30% strain, and (c) VPFPT simulations for the “random” microstructures and the “percolate” microstructure to 30% strain. Major crystallographic directions are labeled for both NaCl (top row) and NaMgF₃ (bottom row) in (a) and are mapped relative to the compression direction in all maps. Pole densities are given in multiples of random distribution (m.r.d.). An m.r.d. of 1 indicates random orientation. Equal area projections.

tion. The (100) maximum extends toward {110} and (001). This extension is seen progressively less as the NaMgF₃ volume percent decreases. For samples with 100% NaMgF₃ content, a small secondary maximum is observed at (001). A small but representative subset of IPFs is shown in Fig. 3a; the full set of IPFs can be found in the appendix of Kaercher (2014).

Texture strength (i.e. maximum pole density) in NaMgF₃ strongly correlates to sample composition (Fig. 4a). While 100% NaMgF₃ samples (white circles) developed very strong CPO with pole densities reaching up to 11.8 m.r.d. (Table 1), samples containing just 15% volume NaCl have pole densities of up to 5.9 m.r.d., i.e. half the texture strength. Whereas texture increased until the final strains in 100% NaMgF₃ samples, texture slightly decreased once $\sim 15\%$ strain was reached in all the two-phase samples (Fig. 4b).

Temperature greatly affected texture development in the 100% NaMgF₃ samples, with pole density maxima reaching 11.8 m.r.d. at 400 °C and 6.9 m.r.d. at 800 °C. On the other hand, temperature had little effect on the two-phase samples. In samples containing 15% NaCl, the maximum pole density of NaMgF₃ at 200 °C was 5.9 m.r.d., and at 400 °C, 5.4 m.r.d. For samples with 25% NaCl or more, the differences in texture strength in NaMgF₃ at different temperatures are negligible (Fig. 4b, Table 1).

The NaCl texture is more irregular and much weaker than the NaMgF₃ texture. Part of this is due to cubic symmetry with inherent multiplicity. The maximum pole densities for NaCl in samples containing 15% NaCl lie near {112} and {110} (the {112} and {110} planes preferentially align perpendicular to compression). At 25% NaCl volume, the pole density maximum at {112} shifts towards

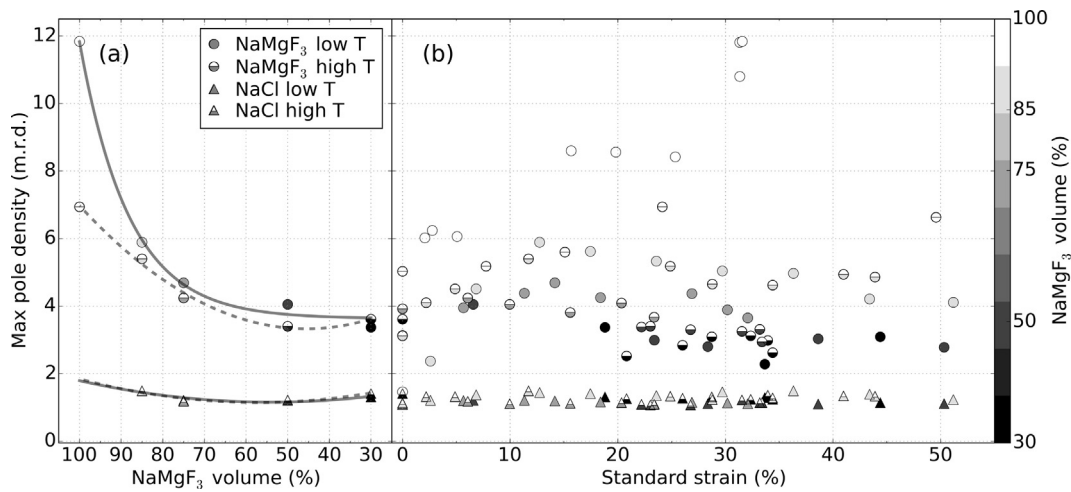


Fig. 4. (a) Scatter plot of maximum IPF pole density versus composition for NaMgF₃ and NaCl for each run (see Table 1 for values). Runs done at higher average temperature are plotted with half-filled shapes, and lower average temperature, with filled shapes. Best-fit curves are shown for higher average temperatures (dashed lines) and lower average temperatures (solid lines) for each phase. (b) Scatter plots of maximum pole density versus standard strain in NaMgF₃ and NaCl. Sample composition shown with gray shade. All points plotted were collected at 20 tons during compression.

Table 2

Statistics for NaMgF₃ and NaCl from X-ray microtomography analysis. The first column in italics gives statistics for the undeformed 75% NaMgF₃ sample. Both percentages measured before sintering (S), and percentages taken from microtomography thresholding (M) are shown.

Run	NaMgF ₃				NaCl			
	<i>–</i>	D1187	D1315	D1316	<i>–</i>	D1187	D1315	D1316
Volume S/M (%)	<i>75/64</i>	75/77	50/50	30/23	25/36	25/23	50/50	70/77
Connectivity (%)	<i>99.98</i>	99.98	99.71	96.25	99.09	95.60	99.79	99.98
Median cluster volume (μm ³)	<i>0.80</i>	1.65	3.30	3.30	1.61	3.02	3.02	1.92
Average aspect ratio	<i>1.25</i>	2.85	3.47	3.61	1.60	3.20	3.29	3.10
Final strain (%)	<i>0</i>	32	33	34	0	32	33	34

{001}, and for 50% and 70% NaCl, the maximum pole density is found at either {001} or {110} (Fig. 3a).

Maximum pole densities in NaCl never reached more than 1.5 m.r.d., nearly an order of magnitude less than the maximum reached in NaMgF₃ (11.8 m.r.d.). Unlike for NaMgF₃, there is little correlation between texture and composition (Fig. 4a). Samples with the least NaCl (15% volume) reached the highest maximum pole density of 1.5 m.r.d., samples with 25% and 50% NaCl reached 1.2 m.r.d., and samples with the most NaCl (70% NaCl) reached 1.4 m.r.d. (Table 1). Neither temperature (Fig. 4a, b) nor strain % (Fig. 4b) appear to correlate with texture in NaCl.

3.3. Microstructure

The spatial distribution of phases, grain cluster sizes, and aspect ratios were quantified with X-ray microtomography for one undeformed 75% NaMgF₃ sample and three samples deformed to 32–34% strain with compositions 75% NaMgF₃ (D1187), 50% NaMgF₃ (D1315), and 30% NaMgF₃ (D1316). Details of deformation conditions for these samples are given in Table 1. Microtomography data was collected from 0.03 mm³ to 0.22 mm³ sub-volumes which may account for some inconsistencies between volume percent measured during sample preparation and microtomography (Table 2). In addition, although great care was taken to threshold phases according to their different absorption intensities during data processing, errors may still arise since NaMgF₃ and NaCl do not drastically differ in intensity (gray shade) and images are a bit blurred.

A cross section taken with microtomography of an undeformed sample with 75% NaMgF₃ and 25% NaCl is shown in Fig. 5a. Because neighboring grains of the same mineral in our samples could not be discerned from each other with phase contrast imaging at microscale resolution, statistics gathered from microtomography

are not of individual grains but rather of interconnected clusters of grains. However, much higher resolution images were collected with an SEM (Fig. 5b). Without true grain size gathered from EBSD, our best estimate of NaCl (white) grain diameter is roughly 1–10 μm, and NaMgF₃ (gray) grain diameter is about 5–20 μm.

Although microtomography has lower resolution than SEM, it can be used to quickly and non-destructively reconstruct 3D images to micron resolution. A 3D reconstruction of a 75% NaMgF₃ undeformed sample and a 75% NaMgF₃ sample deformed to 32% strain (Fig. 6) were made by stacking microtomography slices similar to those shown in Fig. 5a. Compared to the undeformed reconstruction, the deformed reconstruction shows grain clusters shortened in the compression direction and elongated in planes perpendicular to compression; the NaCl appears to fill in between the NaMgF₃ grain clusters (Fig. 6c).

Quantitative results are shown in Table 2. Connectivity is defined here as the percent of the total phase volume contained in the largest, interconnected cluster of grains of that phase and was calculated by dividing the volume of the largest cluster of grains of a phase by the total volume of the phase. Both NaMgF₃ and NaCl in the 75% NaMgF₃ sample are >99% connected before deformation. NaCl may not appear to be highly interconnected in two dimensions, so we include the 3D reconstruction of NaCl only in Fig. 6a to help show that it is. In the 75% NaMgF₃ sample, connectivity of NaMgF₃ remained constant during deformation while connectivity of NaCl decreased. In both phases, grain cluster size increased during deformation. Decreased connectivity and increased clustering of NaCl in the 75% NaMgF₃ sample may be due to NaCl squeezing between NaMgF₃ grain clusters in the planes perpendicular to compression to form sheets while becoming less connected in the compression direction. As expected, the majority of NaMgF₃ and NaCl grain clusters in the undeformed sample have aspect ratio ≈1, while the majority in deformed samples have aspect ratios >1.

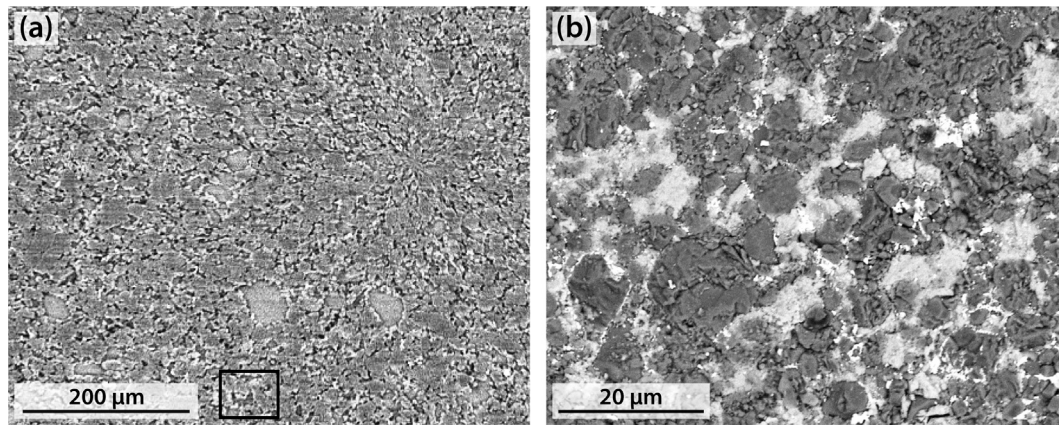


Fig. 5. Cross sectional slices of an undeformed sample with composition 75% NaMgF₃ (darker gray) and 25% NaCl (lighter gray) collected with (a) microtomography and (b) a scanning electron microscope at 1000× magnification. The black rectangle in (a) shows the relative size of the entire area of (b).

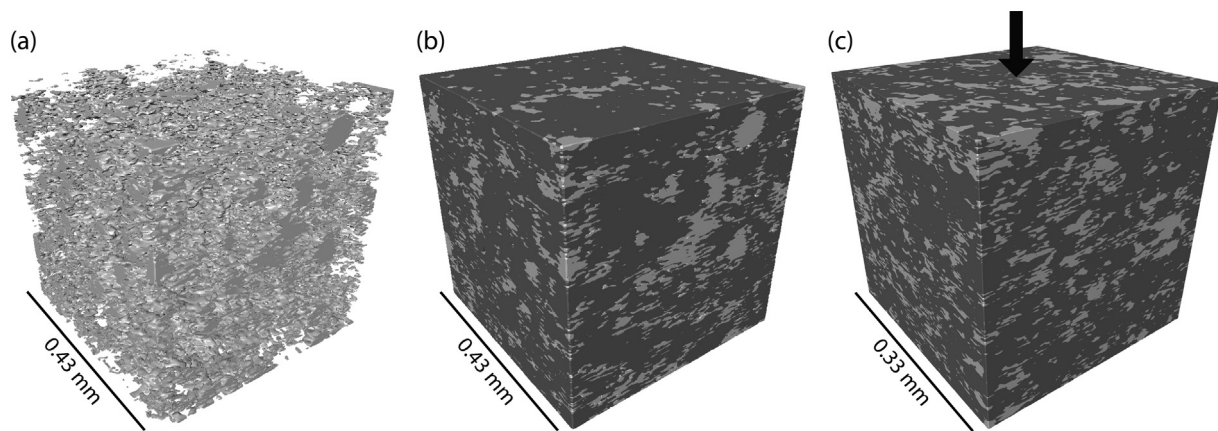


Fig. 6. Three-dimensional microtomography images of (a) NaCl in an undeformed 75% NaMgF₃ sample, (b) both phases in an undeformed 75% NaMgF₃ sample, and (c) both phases in a 75% NaMgF₃ sample deformed to 32% strain. NaMgF₃ grains are shown in darker gray, and NaCl grains are shown in lighter gray. Compression direction indicated by the arrow.

Aspect ratio is the ratio of the longest dimension in 3D of a grain cluster to the shortest dimension.

4. Discussion

4.1. Experimental deformation

4.1.1. Differential stress

Our results suggest that NaCl controls deformation. The average differential stress in 100% NaMgF₃ samples is about 40% greater than in NaMgF₃ in 85% NaMgF₃ samples deformed at similar conditions, suggesting that NaCl absorbs much of the plastic deformation at just 15% volume. In addition, microtomography shows both NaCl and NaMgF₃ to be interconnected in our samples (Table 2).

Differential stress in NaCl is up to an order of magnitude less than in NaMgF₃ in all samples, demonstrating that stress partitions into the stronger NaMgF₃ phase. We show in section 4.2.2 with viscoplastic modeling that strain likely localizes into the weaker NaCl phase. The shape change of NaCl clusters during deformation (Fig. 6c) also suggests that NaCl uptakes much of the strain, but we cannot quantify this from microtomography data since results are of grain clusters rather than single grains. All lower mantle deformation studies discussed here agree that stress partitions into the stronger phase, and strain into the weaker phase, yet not all agree that the weaker phase is interconnected and controls deformation (Madi et al., 2005; Li et al., 2007; Wang et al., 2013; Girard et al., 2016; Miyagi and Wenk, 2016).

Disagreement among these studies about which phase controls deformation may stem from differences in final strain. Madi et al. (2005) and Wang et al. (2013) deformed aggregates to 15% and 20% bulk strain, respectively, and found the stronger perovskite phase controls deformation. However, Madi et al. (2005) mention that ferropericlase begins to form layers or “pancakes” perpendicular to compression much like we see in NaCl (Fig. 6c) at higher strain. Similarly, Girard et al. (2016) shows flattened ferropericlase grains at their final 100% bulk strains and suggest that the stronger phase controls deformation at lower strains (<20%), but the weaker phase controls deformation at higher strains. We see a reduction of differential stress in NaMgF₃ with the addition of NaCl already at strains <10% (Fig. 2b) suggesting that NaCl accommodates a large portion of differential stress even at low strains.

Starting microstructure may also influence which phase controls deformation, but the relationship between phase connectivity and which phase controls deformation is not clear-cut: there are examples of the strong phase controlling deformation when the weak phase is interconnected (e.g. Madi et al., 2005), and the weak phase controlling deformation when it is not interconnected (e.g. Girard et al., 2016).

The controlling phase may also be determined by phase strength contrast. Estimated strength contrast is greater in studies that find that the weak phase controls deformation (Girard et al., 2016; Li et al., 2007, this study) compared to studies that find the stronger perovskite phase controls deformation (Madi et al., 2005; Wang et al., 2013). Here NaCl controls deformation at only 15% vol-

ume, which may be due to a higher strength contrast for NaMgF₃–NaCl compared to other composites mentioned here. Then again Li et al. (2007) and Girard et al. (2016) may have found ferropericline controls deformation at only 15% volume as well, but they had no samples with ferropericline volume between 0 and 25%.

Differential stress in NaCl is about the same for all compositions whereas differential stress in NaMgF₃ decreases with increasing NaCl content (Fig. 2b). Thus the stress becomes more evenly distributed among the two phases as NaCl content increases and bears more of the strain, modulating the stress. This is consistent with NaMgF₃ becoming less interconnected (Table 2), thus having less contact with the pistons and bearing less of the load. Temperature also causes stress to be more homogeneously distributed among the two phases (Fig. 2a).

Strain hardening is observed in both NaMgF₃ and NaCl until ~10–15% followed by no overall trend of either strain hardening or strain weakening in either phase during steady state deformation (Fig. 2a). By comparison, Girard et al. (2016) observed strain hardening in aggregates up to 20% strain, followed by a hint of strain weakening in bridgmanite to their final strain of ~100%. It is possible that Girard et al. (2016) sees strain weakening because they deformed samples in shear, while we deformed our samples under uniaxial compression. Shear localization may occur in both cases but is less likely to lead to strain weakening in compression because shear bands do not tend to align with each other as much as they do in shear strain.

4.1.2. Texture

We find a (100) maximum in NaMgF₃ at all conditions in all samples. A secondary maximum at (001) and extension of the (100) maximum toward {110} and (001) is observed in NaMgF₃ in samples with little or no NaCl. It is unclear if this texture is similar to that of bridgmanite at mantle conditions. While some DAC experiments report little to no CPO development in bridgmanite (Meade et al., 1995; Merkel et al., 2003), others suggest bridgmanite develops significant texture that varies depending on the starting material. For example, a (001) transformation texture was observed in bridgmanite just after conversion from enstatite that remained up to 56 GPa (Miyagi and Wenk, 2016). Wenk et al. (2004) and Miyagi and Wenk (2016) both saw a (100) transformation texture in bridgmanite immediately after converting from olivine or ringwoodite to bridgmanite + ferropericline. Yet Wenk et al. (2004) found a subsequent weak {012} deformation texture while Miyagi and Wenk (2016) saw a (001) deformation texture at lower pressure followed by a (100) maximum at pressure >55 GPa. If bridgmanite develops a (100) deformation texture in the lower mantle due to dislocation creep, then NaMgF₃ is a good analog. We explore likely slip systems in NaMgF₃ in the next section.

NaCl in samples with at least 25% NaCl acquire pole density maxima at {001} or {101} in IPFs (Fig. 4), consistent with previous uniaxial compression studies of NaCl (e.g. Franssen, 1994) and polycrystalline ferropericline deformed in a DAC (Merkel et al., 2002). However, samples containing <25% NaCl instead acquire weak maxima at {112} and {101}. A similar texture was observed for ferropericline in bridgmanite–ferropericline assemblages deformed in the DAC and was attributed to heterogeneous deformation (Wenk et al., 2004; Miyagi and Wenk, 2016). Weak ferropericline textures were also observed by Wang et al. (2013). Under simple shear deformation, texture development may be even weaker than in compression experiments. Wenk et al. (2009) showed that weak texture is observed for NaCl deformed in plain shear because crystals continue to rotate without converging on a single component.

Temperature greatly reduced CPO in the 100% NaMgF₃ samples, possibly due to additional slip systems becoming more active at higher temperature, thereby decreasing the (100) texture of

NaMgF₃ (e.g. Poirier et al., 1989) or possibly by decreased dislocation mechanisms and increased diffusion. The effect of temperature on two-phase samples was much less and even negligible in samples containing 50% NaCl or more. Temperature may have less effect on texture in two-phase samples due to NaCl pinning grain boundaries of NaMgF₃ and thereby limiting dislocation climb and glide at both lower and higher temperatures (e.g. Herwegh and Berger, 2004). Alternatively, it could be that NaCl absorbs the same amount of deformation without developing significant CPO at both low and high temperatures, leaving less to be accommodated by dislocation slip in NaMgF₃.

As stress builds in NaMgF₃, it begins to deform plastically, initiating dislocation slip. On the other hand, NaCl has lower elastic constants and does not support as much stress as NaMgF₃. It also develops a much weaker texture either because it deforms by a mechanism that does not produce crystallographic CPO, or it may be deforming heterogeneously between neighboring NaMgF₃ grains and so does not acquire an overall CPO.

4.2. Polycrystal plasticity simulations

4.2.1. Self-consistent model (VPSC)

We performed viscoplastic self-consistent (VPSC) modeling (Lebensohn and Tomé, 1993) to investigate likely slip system activities during experiments. VPSC allows grain inclusions of multiple phases to deform by dislocation slip in a homogeneous medium that has the average properties of the composite (Eshelby, 1957). Deformation and rotation of grains depends on their orientation relative to compression and the relative critical resolved shear stress (CRSS) of the slip systems. By comparing textures produced by VPSC simulations with experimental textures, we can estimate slip systems that were active during the experiment.

In our VPSC models, 2000 grains of each NaMgF₃ and NaCl, present in various volume percent, were compressed to 30% equivalent strain in 1% increments. Grains of both NaMgF₃ and NaCl had little to no texture before deformation in experiments, and thus were prescribed a random orientation distribution at the start of VPSC simulations. A stress exponent of $n = 3$ was assumed (Frost and Ashby, 1982).

Our first approximation of slip system activity in NaMgF₃ assumed that slip on (100) produced the pole density maximum seen at (100) in experimental IPFs (Fig. 3a). Thus we assigned (100)[010] and (100)(011) slip systems the lowest relative CRSS of 0.5, and varied relative CRSS of additional slip systems until we found the closest match to experimental texture as possible. Relative CRSS and resulting slip system activities are listed in Table 3. Because twinning is common in perovskite-structured minerals, we also modeled twinning of {110}{111} with VPSC, which produced a very weak maximum at 100, and thus may slightly contribute to the (100) pole density maximum (Fig. 4b). No combination of slip systems reproduced both the maximum at (100) and the secondary maximum at (001) seen in 100% NaMgF₃, which suggests a small degree of strain heterogeneity in single phase NaMgF₃. We are not aware of any previous studies of slip systems in NaMgF₃ with which we can compare results here. However, similar to our results for NaMgF₃, Miyagi and Wenk (2016) suggest preferential slip on (100)[010] or (100)(011) in bridgmanite above 55 GPa. Numerical models also find slip on (100) most likely at higher pressure (Mainprice et al., 2008; Kraych et al., 2016).

VPSC results with slip on {110}{111} show a closest match to experimental NaCl textures with maxima at {100} and {110} (Fig. 3b) in agreement with studies of slip during uniaxial compression in NaCl (e.g. Franssen, 1994) and in (Mg, Fe)O (e.g. Merkel et al., 2002; Kaercher et al., 2012). The slip systems {110}{111} and {110}{111} have equal Schmidt factors and rotate crystallographic

Table 3
Relative CRSS of MgSiO₃ and MgO inferred from CPO observations for pressures of >35 GPa obtained in DAC (Wenk et al., 2011) compared to relative CRSS assigned to slip systems for NaMgF₃ and NaCl inferred with VPSC in this study. Activity percentages are listed for NaMgF₃ (left side) and NaCl (right side) following 30% axial shortening for various sample compositions and random (R) and percolate (P) VPFFT microstructures corresponding to IPFs in Fig. 3b, c.

Slip systems		(100) [010]	(100) (011)	(010) (101)	(001) [100]	(001) [010]	(001) (110)	{111} (101)	Tot (%)	MgO	{111} (101)	{110} (110)	{100} (011)	Tot (%)
CRSS	MgSiO ₃	3	4	–	1	1	1	–		MgO	0.75	0.50	1.00	
	NaMgF ₃	0.5	0.5	10	5	5	5	50		NaCl	2.50	0.25	3.00	
VPSC act (%)	25%vol	2.5	13.6	0.0	0.0	0.2	0.2	0.0	16.5	75%vol	8.2	63.9	11.4	83.5
	75%vol	7.8	51.4	0.2	0.1	1.7	2.1	0.0	63.3	25%vol	5.6	23.3	7.9	36.8
	100%vol	10.2	79.3	0.4	0.1	4.4	5.4	0.2	100.0	0%vol	–	–	–	–
VPFFT act (%)	R 25% vol	1.7	10.3	0.1	0.0	1.3	1.5	0.1	14.9	R 75%vol	12.9	53.9	18.4	85.1
	R 75%vol	5.9	40.3	0.7	0.1	7.2	8.3	2.4	64.9	R 25%vol	6.9	18.3	10.0	35.1
	R 100%vol	8.1	58.0	1.1	0.1	1.6	13.4	7.8	100.0	R 0%vol	–	–	–	–
	P 75%vol	5.6	38.0	0.4	0.1	4.7	5.5	0.6	54.8	P 25%vol	10.4	19.6	15.2	45.2

planes in opposite directions, essentially canceling each other and so are not expected to produce texture. However, a VPSC study of NaCl that takes grain shape into account showed that texture increasingly develops with deformation as grain aspect ratios increase (Wenk et al., 1989).

Pole density maxima predicted by VPSC for both NaMgF₃ and NaCl decreased with the addition of NaCl, but not as much as observed in experiments (Fig. 3a, b). VPSC overestimates pole densities likely because it assumes that all deformation occurs by dislocation glide and does not take into account interaction between grains of different phases having different elastic and plastic properties, shapes, and crystallographic orientations. Thus VPSC simulations, which only consider the interaction among individual grains and the homogeneous equivalent medium, underestimate stress and strain heterogeneity and are not ideal for modeling two-phase deformation.

4.2.2. Viscoplastic model using fast Fourier transform (VPFFT)

We also modeled two-phase viscoplastic deformation with a method that uses fast Fourier transforms (VPFFT) and Greens functions to solve the governing equations for stress and strain rate in response to an applied strain at regularly-spaced grid points in a chosen 3D microstructure (Lebensohn, 2001). Individual grain orientations, shapes, grain–grain interactions, and intragranular heterogeneity of the micromechanical fields are considered, making it well-suited for simulating deformation in a heterogeneous two-phase composite.

Three periodic “random” microstructures with equant grains of NaMgF₃ and NaCl present in different volume percent (100% NaMgF₃, 75% NaMgF₃–25% NaCl and 50% NaMgF₃–50% NaCl), and one “percolate” microstructure with 25% volume NaCl sitting as veins between equant NaMgF₃ grains were created using Voronoi tessellations (Voronoi, 1908) and are shown in Fig. 7. NaCl grains were made roughly five times smaller than NaMgF₃ grains based on relative grain sizes seen in Fig. 5b. The 3D grain maps were discretized into a 64 × 64 × 64 grid of Fourier points. In the 75% NaMgF₃ random microstructure, 96.4% of NaCl Fourier points are contained in one interconnected grain cluster, and in the 25% NaMgF₃ random and 75% NaMgF₃ percolate microstructures, NaCl Fourier points are 100% interconnected, similar to experimental microstructures (Table 2). Grains may shorten but must maintain constant volume (e.g. they cannot break or grow), and connectivity does not change during deformation in these simulations. Initial orientation of grains was assigned as random to be consistent with experimental observations. The same relative CRSS used in VPSC simulations (Table 3) were assigned here as well. Stress was defined as axial compressive to a total strain of 30% in increments of 2% strain.

While the 75% NaMgF₃ “random” microstructure IPF (Fig. 3c) shares the (100) pole density maximum seen in the experimental 75% NaMgF₃ IPF (Fig. 3a), the “percolate” microstructure IPF (Fig. 3c) shares the extension of the (100) NaMgF₃ maximum toward {110} and a secondary maximum that resembles the extension towards (001) and more accurately matches the maximum pole densities for both NaMgF₃ and NaCl. This suggests a hybrid of “random” and “percolate” microstructures in experimental samples, conceivably with the majority of clusters of NaCl lying in planes perpendicular to compression and thinner and fewer networks of NaCl connecting these planes, similar to the deformed microstructure seen in Fig. 6c.

VPFFT predicts similar slip system activities as VPSC for “random” microstructures, but with slightly more homogeneously distributed slip activity (Table 3). This correlates with smoother textures in VPFFT IPFS, because in contrast to VPSC simulations in which every point in a grain experiences the same plastic distortion, VPFFT allows deformation states among points in the same grain to deviate from each other. Other differences arise from VPFFT providing exact solutions while VPSC approximates non-linear behavior with a linearization scheme (Lebensohn et al., 2016). The smoother textures predicted by the VPFFT model more closely match experimental two-phase aggregate textures, while sharper VPSC textures more closely resemble experimental 100% NaMgF₃ textures (Fig. 3).

In both VPSC and random microstructure VPFFT simulations, the percent of deformation accommodated by secondary slip systems in NaMgF₃ increases with increasing NaMgF₃ content (Table 3). However this increased activity of secondary slip systems in the random 100% NaMgF₃ and 75%NaMgF₃ microstructures fails to reproduce the extension of the (100) maximum toward {110} and (001) seen in the experimental NaMgF₃ IPFs (Fig. 3). Instead in the VPFFT microstructures with the least amount of secondary slip system activity, 25% NaMgF₃ random and 75% NaMgF₃ percolate microstructures, acquire the extension of the (100) maximum towards {110} and (001), suggesting that the extension becomes more pronounced if deformation is accommodated by slip solely on (100). Results for the “percolate” microstructure show much greater activity in NaCl compared with the random microstructure (Table 3) showing it accommodates a greater percent of the total deformation as a thin network.

The relationship between microstructure, strain rate, and stress is best viewed as 2D slices rather than as 3D projections, thus in Fig. 7 we show slices through the 3D microstructure along with associated maps of von Mises equivalent strain rates and stresses shown as scalar quantities. Strain rate maps in Fig. 7 (middle row) show that strain partitions into the weaker NaCl, especially in the “percolate” microstructure. This agrees with flow laws outlined by Handy (1994) that predict strain localization in the weak

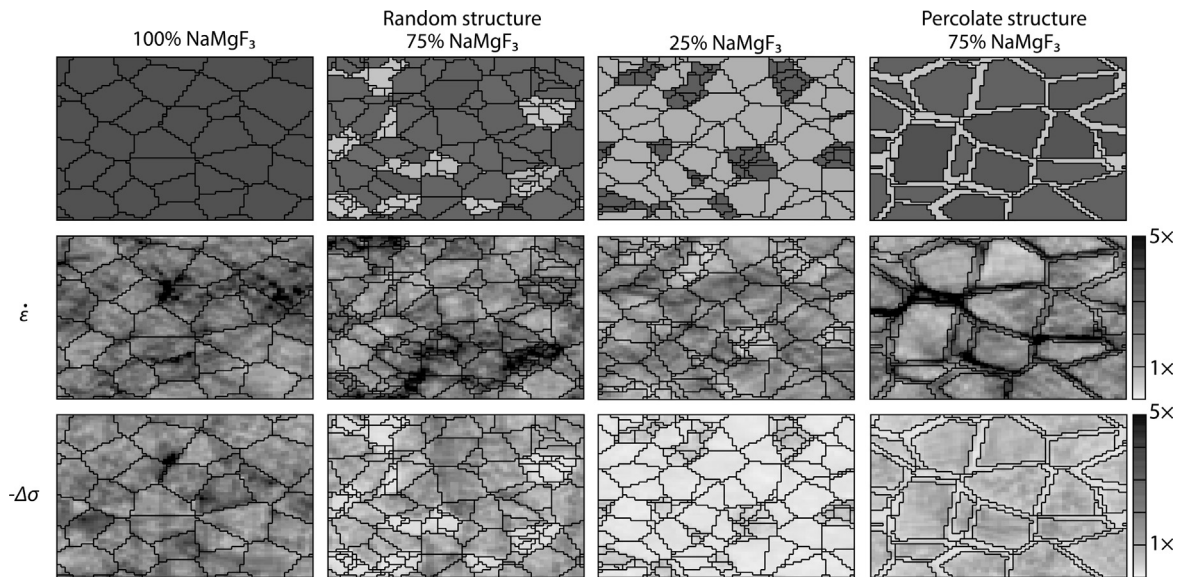


Fig. 7. Maps of VPFPT microstructures with darker gray NaMgF₃ grains and lighter gray NaCl grains (top row), average strain rate ($\dot{\epsilon}$) maps (middle row), and average stress maps ($-\Delta\sigma$) (bottom row) with fastest strain rates and highest stresses shown in black. Homogeneously deformed to 30% strain.

phase in aggregates with an interconnected weak layer (IWL) microstructure. In such structures, the strain rate in the weak phase correlates to the strength contrast and volume percent of the two phases. Strain rate is most heterogeneous in NaCl in two-phase samples with higher NaMgF₃ volume percent, especially in the “percolate” microstructure, which may help explain the weak and irregular textures seen in NaCl IPFs. Strain rates are greatest and most heterogeneous in NaMgF₃ in the 100% NaMgF₃ sample. The greater heterogeneity may be responsible for the secondary maximum that appears at (001) in the 100% NaMgF₃ random microstructure IPF.

Stress maps in the bottom row of Fig. 7 show that NaMgF₃ supports more stress than NaCl in all samples, which we also observed in experiments. Stress is greatest and most heterogeneous in NaMgF₃ in the 100% NaMgF₃ sample. Differential stresses were calculated for each phase in all microstructures, and we find that the model underestimates the ratio of differential stress ($-\Delta\sigma_{\text{NaMgF}_3}/-\Delta\sigma_{\text{NaCl}}$) supported in two-phase samples compared with experiments: $-\Delta\sigma_{\text{NaMgF}_3}/-\Delta\sigma_{\text{NaCl}}$ in the 25% NaMgF₃ and 75% NaMgF₃ random microstructures is 2.47 and 6.06, respectively, and in the 75% NaMgF₃ percolate microstructure, 3.35; in comparison $-\Delta\sigma_{\text{NaMgF}_3}/-\Delta\sigma_{\text{NaCl}}$ for maximum stresses in experimental samples 30% NaMgF₃ and 75% NaMgF₃ is 4.13 and 8.71, respectively.

Here we focus on dislocation slip as the active deformation mechanism, but it should be mentioned that the lack of CPO development in NaCl, its small grain size ($\leq 1 \mu\text{m}$) seen with SEM (Fig. 5b), and change in connectivity and grain cluster size of NaCl during deformation (Table 2, Fig. 6) may suggest grain-size sensitive creep mechanisms accommodated by grain boundary sliding. Likewise, previous studies have found deformation controlled by secondary phases occurs by Nabarro–Herring creep and/or Coble creep due to grain growth being limited by a secondary phase (e.g. calcite–anhydrite, Barnhoorn et al., 2005). However, flattened grain clusters seen in Fig. 6c suggest the sample deformed by plasticity, not by diffusion creep. The weak texture of NaCl may well result from heterogeneous deformation by dislocation slip and not lack of dislocation slip. It is also possible that the dominant deformation regime evolves with strain and microstructural changes. For example, Li et al. (2007) argue for MgO deforming in power law creep by dynamic recrystallization, and because of the presence of a sec-

ond phase, grain size is reduced, so they suggest there may be a switch to grain-size sensitive creep.

4.3. Implications for the lower mantle

At axial strains up to 51%, CPO in the bridgmanite analog, NaMgF₃, was notably lower in two-phase samples compared with single phase NaMgF₃ (Fig. 4b), which suggests that weaker phases, like ferropericlase, may absorb deformation without significantly contributing to CPO and in fact will likely reduce CPO in the perovskite phase. This may explain the lack of anisotropy in the lower mantle. This view differs somewhat from that of Girard et al.’s (2016), which suggests that deformation is localized (based on observed strain weakening in their samples) leaving the majority of the lower mantle undeformed and thus without CPO and anisotropy. However, we do not see strain weakening here despite the larger rheology contrast between NaMgF₃ and NaCl compared to bridgmanite and ferropericlase. Even so, strain weakening may still occur in areas of high simple shear strain as opposed to areas of pure shear strain.

We find lower differential stress at all strains (Fig. 2b) in two-phase samples compared to single phase NaMgF₃ suggesting that weaker ferropericlase will reduce lower mantle strength even at low strains. This suggests by analogy that MgO may play a major role in determining lower mantle strength. If MgO is the deformation controlling phase in the lower mantle, it will not only affect CPO but also determine viscosity and affect geodynamical processes such as plate motion (Tackley, 2000), slab subduction and stagnation (Marquardt and Miyagi, 2015), mantle plumes and hotspots (French and Romanowicz, 2015), and relatedly, variation in ocean island basalt geochemistry (Li et al., 2014).

As discussed above, analog minerals may deform differently elastically and plastically than their lower mantle counterparts. For example, differences in slip system activities between analogs and lower mantle minerals could result in a different seismic signature if CPO develops. Partitioning of stress and strain in bridgmanite and ferropericlase may vary from that of NaMgF₃ and NaCl depending on strength contrast at lower mantle conditions. In addition our starting microstructure for 75% NaMgF₃–25% NaCl samples had NaCl already highly interconnected, whereas a eutectoid microstructure is expected at the top of the lower mantle after dissociation from Mg₂SiO₄ phases. However, even in the case of

a starting microstructure with isolated ferropericlasite, it may still control deformation (Girard et al., 2016). Conditions in the lower mantle, such as strain rate, grain sizes, and temperature, which affect deformation, may differ from those in our experiments. For example, slip is less active at lower strain rate in NaCl (Carter and Heard, 1970) and MgO (Routbort, 1979), which suggests that CPO may be even less in the lower mantle (strain rates of $\sim 10^{-14} \text{ s}^{-1}$) than in D-DIA experiments ($\sim 10^{-3} \text{ s}^{-1}$). Calculations of grain sizes in the upper-most lower mantle that take into account Zener pinning during two-phase growth by grain-boundary diffusion estimates grain sizes on the order of 100–1000 μm (Solomatov et al., 2002), which is 1 to 2 orders of magnitude larger than grains in our experiments and may result in grain-size independent mechanisms, such as dislocation creep, being more active (e.g. Frost and Ashby, 1982) and may enhance CPO. At higher temperatures, dislocation creep may become less active or may, on the other hand, lead to larger grain growth making dislocation creep more active. Results here indicate that temperature did not greatly affect CPO development in two-phase samples, but has a stronger effect on aggregate strength (Fig. 2b).

5. Conclusion

We present evidence that ferropericlasite may become interconnected in the lower mantle, leading to reduced viscosity and weakening of CPO. These results reiterate the importance of including the effect of secondary phase ferropericlasite on rheology in geophysical models of the lower mantle.

While our results strongly suggest reduction of CPO due to ferropericlasite controlling deformation, results presented here cannot constrain which deformation mechanism is responsible for CPO reduction. Future systematic deformation experiments on bridgmanite–ferropericlasite aggregates coupled with *in situ* microtomography and/or *ex situ* electron microscopy may help to construct deformation maps that can be extrapolated to better constrain likely deformation mechanisms in the lower mantle. Such experiments are becoming increasingly feasible (with larger, more easily recoverable samples) thanks to increased pressure range of large volume presses (T-cups, Drickamer, D-DIA). Alternatively two-phase deformation of lower mantle minerals may be predicted by comprehensive models that allow for not only dislocation slip but also grain nucleation, grain growth, grain-boundary migration and lattice diffusion creep. In addition, the effects of starting microstructure, strength contrast, and aggregate strain should be looked at more closely. The starting microstructure here had NaMgF_3 and NaCl already highly connected. Future experiments should be done to compare results for samples with different starting microstructures. As shown here, the viscoplastic fast Fourier transform-based approach is a valuable tool for predicting stress and strain partitioning and CPO development in polyphase samples with different starting microstructures. We compare results here to previous studies to examine the role strength contrast between the two phases plays in determining the deformation-controlling phase and suggest that this may evolve with strain, but more systematic studies are necessary. Modeling of two-phase deformation using VPPFT or finite element methods may be best suited for this pursuit as well.

Acknowledgements

This work was supported by CDAC and NSF grant EAR-1343908, NSF/CSEDI 1067513. LM acknowledges support from CDAC and NSF grant EAR-1344579. YW acknowledges support from NSF grant EAR-136127. Portions of this work were performed at GeoSoilEnviroCARS (Sector 13) and beamline 2-BM-B (XOR) of the Advanced Photon Source (APS), Argonne National Laboratory. We thank the

Advanced Light Source (ALS) of the Lawrence Berkeley National Laboratory (LBNL) for the use of beamline 8.3.2. P. Kaercher is grateful to David Martin for providing a beautiful sample of neighborite and to James Wu for his help in synthesizing neighborite. All authors greatly appreciate the constructive comments from all three reviewers.

Appendix A. Supplementary material

Supplementary material related to this article can be found online at <http://dx.doi.org/10.1016/j.epsl.2016.09.030>.

References

- Amodeo, J., Carrez, P., Cordier, P., 2012. Modelling the effect of pressure on the critical shear stress of MgO single crystals. *Philos. Mag.* 92, 1523–1541. <http://dx.doi.org/10.1080/14786435.2011.652689>.
- Barnhoorn, A., Bystricky, M., Kunze, K., Burlini, L., Burg, J.P., 2005. Strain localization in biminerale rocks: experimental deformation of synthetic calcite-anhydrite aggregates. *Earth Planet. Sci. Lett.* 240, 748–763.
- Carter, N.L., Heard, H.C., 1970. Temperature and rate dependent deformation of halite. *Am. J. Sci.* 269, 193–249.
- Cordier, P., Ungár, T., Zsoldos, L., Tichy, G., 2004. Dislocation creep in MgSiO_3 perovskite at conditions of the Earth's uppermost lower mantle. *Nature* 428, 837–840.
- Cottaar, S., Li, M., McNamara, A., Wenk, H.R., Romanowicz, B., 2014. Synthetic seismic anisotropy models within a slab impinging on the core-mantle boundary. *Geophys. J. Int.* 199 (1), 164–177.
- Day, R.B., Stokes, R.J., 1966. Mechanical behavior of polycrystalline magnesium oxide at high temperatures. *J. Am. Ceram. Soc.* 49 (7), 345–354.
- Eshelby, J.D., 1957. The determination of the elastic field of an ellipsoidal inclusion, and related problems. *Proc. R. Soc. A, Math. Phys. Eng. Sci.* 241 (1226), 376–396.
- Franssen, R.C.M.W., 1994. The rheology of synthetic rocksalt in uniaxial compression. *Tectonophysics* 233, 1–40.
- French, S.W., Romanowicz, B.A., 2014. Whole-mantle radially anisotropic shear velocity structure from spectral-element waveform tomography. *Geophys. J. Int.* 199, 1303–1327.
- French, S.W., Romanowicz, B.A., 2015. Broad plumes rooted at the base of the Earth's mantle beneath major hotspots. *Nature* 525, 95–99.
- Frost, H.J., Ashby, M.F., 1982. *Deformation-Mechanism Maps: The Plasticity and Creep of Metals and Ceramics*. Pergamon Press, New York.
- Girard, J., Amulele, G., Farla, R., Mohiuddin, A., Karato, S.I., 2016. Shear deformation of bridgmanite and magnesio-wüstite aggregates at lower mantle conditions. *Science* 351 (6269), 144–147.
- Handy, 1994. Flow laws for rocks containing two non-linear viscous phases: a phenomenological approach. *J. Struct. Geol.* 16 (3), 287–301.
- Herwegh, M., Berger, A., 2004. Deformation mechanisms in second-phase affected microstructures and their energy balance. *J. Struct. Geol.* 26, 1483–1498.
- Irifune, T., Tsuchiya, T., 2007. Mineralogy of the Earth—phase transitions and mineralogy of the lower mantle. In: *Treatise on Geophysics*, vol. 2, pp. 33–62.
- Kaercher, P.M., 2014. Crystallographic preferred orientation and deformation of deep Earth minerals. Dissertation. University of California, Berkeley.
- Kaercher, P., Speziale, S., Miyagi, L., Kaniptyacharoen, W., Wenk, H.R., 2012. Crystallographic preferred orientation in wüstite (FeO) through the cubic-to-rhombohedral phase transition. *Phys. Chem. Miner.* 39, 613–626.
- Karato, S.I., Zhang, S., Wenk, H.R., 1995. Superplasticity in Earth's lower mantle: evidence from seismic anisotropy and rock physics. *Science* 270 (5235), 458–461.
- Kraych, A., Carrez, P., Hirel, P., Clouet, E., Cordier, P., 2016. On dislocation glide in MgSiO_3 bridgmanite at high-pressure and high-temperature. *Earth Planet. Sci. Lett.* 452, 60–68. <http://dx.doi.org/10.1016/j.epsl.2016.07.035>.
- Lebensohn, R.A., 2001. N-site modeling of a 3D viscoplastic polycrystal using fast Fourier transform. *Acta Mater.* 49, 2723–2737.
- Lebensohn, R.A., Tomé, C.N., 1993. A self-consistent anisotropic approach for the simulation of plastic deformation and texture development of polycrystals: application to zirconium alloys. *Acta Metall. Mater.* 9, 2611–2624.
- Lebensohn, R.A., Zecevic, M., Knezevic, M., McCabe, R.J., 2016. Average intragranular misorientation trends in polycrystalline materials predicted by a viscoplastic self-consistent approach. *Acta Mater.* 104, 228–236.
- Lewis, M.H., Bright, M.W.A., 1971. Transformation twinning in synthetic neighborite. *Am. Mineral.* 56, 1519–1526.
- Li, L., Addad, A., Weidner, D., Long, H., Chen, J., 2007. High pressure deformation in two-phase aggregates. *Tectonophysics* 439, 107–117.
- Li, M., McNamara, A.K., Garner, E.J., 2014. Chemical complexity of hotspots caused by cycling oceanic crust through mantle reservoirs. *Nat. Geosci.* 7, 366–370.
- Liu, L., Bi, Y., Xu, J., Chen, X., 2010. Ab initio study of the elastic properties of sodium chloride at high pressure. *Physica B* 405, 2175–2180.
- Lutterotti, L., Vasin, R., Wenk, H.R., 2014. Rietveld texture analysis from synchrotron diffraction images. I: calibration and basic analysis. *Powder Diffr.* 29 (1), 76–84.

- Madi, K., Forest, S., Cordier, P., Boussuge, M., 2005. Numerical study of creep in two-phase aggregates with a large rheology contrast: implications for the lower mantle. *Earth Planet. Sci. Lett.* 237, 223–238.
- Mainprice, D., Tommasi, A., Ferré, D., Carrez, P., Cordier, P., 2008. Predicted glide systems and crystal preferred orientations of polycrystalline silicate Mg–perovskite at high pressure: implications for the seismic anisotropy in the lower mantle. *Earth Planet. Sci. Lett.* 271, 135–144.
- Marquardt, H., Miyagi, L., 2015. Slab stagnation in the shallow lower mantle linked to an increase in mantle viscosity. *Nat. Geosci.* 8 (4), 311–314.
- Martinez, I., Wang, Y., Guyot, F., Liebermann, R.C., 1997. Microstructures and iron partitioning in (Mg,Fe)SiO₃ perovskite–(Mg,Fe)O magnesiowüstite assemblages: an analytical transmission electron microscopy study. *J. Geophys. Res.* 102 (B3), 5265–5280.
- McNamara, A.K., van Keken, P.E., Karato, S.I., 2002. Development of anisotropic structure in the Earth's lower mantle by solid-state convection. *Nature* 415, 310–314.
- Meade, C., Silver, P.G., Kaneshima, S., 1995. Laboratory and seismological observations of lower mantle isotropy. *Geophys. Res. Lett.* 22 (10), 1293–1296.
- Merkel, S., Wenk, H.R., Badro, J., Montagnac, G., Gillet, P., Mao, H.K., Hemley, R.J., 2003. Deformation of (Mg_{0.9},Fe_{0.1})SiO₃ perovskite aggregates up to 32 GPa. *Earth Planet. Sci. Lett.* 209, 351–360.
- Merkel, S., Wenk, H.R., Shu, J., Shen, G., Gillet, P., Mao, H.K., Hemley, R.J., 2002. Deformation of polycrystalline MgO at pressures of the lower mantle. *J. Geophys. Res.* 107 (B11), 2271.
- Miyagi, L.M., Wenk, H.R., 2016. Texture development and slip systems in bridgmanite and bridgmanite + ferropericlaase aggregates. *Phys. Chem. Miner.* <http://dx.doi.org/10.1007/s00269-016-0820-y>.
- Poirier, J.P., Beauchesne, S., Guyot, F., 1989. Deformation mechanisms of crystals with perovskite structure. In: Navrotsky, A., Weidner, D.J. (Eds.), *Perovskite: A Structure of Great Interest to Geophysics and Materials Science*. In: AGU Geophysical Monograph Series, vol. 45, pp. 119–123.
- Routbort, J.L., 1979. Work hardening and creep of MgO. *Acta Metall.* 27, 649–661.
- Solomatov, V.S., El-Khozondar, R., Tikare, V., 2002. Grain size in the lower mantle: constraints from numerical modeling of grain growth in two-phase systems. *Phys. Earth Planet. Inter.* 129, 265–282.
- Tackley, P.J., 2000. Mantle convection and plate tectonics: toward an integrated physical and chemical theory. *Science* 288, 2002–2006.
- Umemoto, K., Wentzcovitch, R.M., 2011. Two-stage dissociation in MgSiO₃ post-perovskite. *Earth Planet. Sci. Lett.* 311, 225–229.
- Umemoto, K., Wentzcovitch, R.M., Weidner, D.J., Parise, J.B., 2006. NaMgF₃: a low-pressure analog of MgSiO₃. *Geophys. Res. Lett.* 33, L15304.
- Voronoi, G.F., 1908. Nouvelles applications des paramètres continus à la théorie de formes quadratiques. *J. Reine Angew. Math.* 134, 198–287.
- Wang, Y., Durham, W., Getting, I.C., Weidner, D.J., 2003. The deformation-DIA: a new apparatus for high temperature triaxial deformation to pressures up to 15 GPa. *Rev. Sci. Instrum.* 74 (6), 3002–3011.
- Wang, Y., Guyot, F., Yeganeh-Haeri, A., Liebermann, R.C., 1990. Twinning in MgSiO₃ perovskite. *Science* 248, 468–471.
- Wang, Y., Hilaret, N., Nishiyama, N., Yahata, N., Tsuchiya, T., Morard, G., Fiquet, G., 2013. High-pressure, high-temperature deformation of CaGeO₃ (perovskite) MgO aggregates: implications for multiphase rheology of the lower mantle. *Geochem. Geophys. Geosyst.* 14 (9), 3389–3408.
- Wenk, H.R., Armann, M., Burlini, L., Kunze, K., Bortolotti, M., 2009. Large strain shearing of halite: experimental and theoretical evidence for dynamic texture changes. *Earth Planet. Sci. Lett.* 280, 205–210.
- Wenk, H.R., Canova, G., Molinari, A., Mecking, H., 1989. Texture development in halite: comparison of Taylor model and self-consistent theory. *Acta Metall.* 37 (7), 2017–2029.
- Wenk, H.R., Cottaar, S., Tomé, C., McNamara, A., Romanowicz, B., 2011. Deformation in the lowermost mantle: from polycrystal plasticity to seismic anisotropy. *Earth Planet. Sci. Lett.* 306, 33–45.
- Wenk, H.R., Lonardelli, I., Pehl, J., Devine, J., Prakapenka, V., Shen, G., Mao, H.K., 2004. In situ observation of texture development in olivine, ringwoodite, magnesiowüstite and silicate perovskite at high pressure. *Earth Planet. Sci. Lett.* 226, 507–519.
- Wenk, H.R., Speziale, S., McNamara, A.K., Garnero, E.J., 2006. Modeling lower mantle anisotropy development in a subducting slab. *Earth Planet. Sci. Lett.* 245, 302–314.
- Yamazaki, D., Karato, S.I., 2001. Some mineral physics constraints on the rheology and geothermal structure of Earth's lower mantle. *Am. Mineral.* 86, 385–391.
- Yamazaki, D., Yoshino, T., Nakakuki, T., 2014. Interconnection of ferro-periclaase controls subducted slab morphology at the top of the lower mantle. *Earth Planet. Sci. Lett.* 403, 352–357.
- Zhao, Y., Weidner, D.J., 1993. The single crystal elastic moduli of neighborite. *Phys. Chem. Miner.* 20, 419–424.
- Zhao, Y., Weidner, D.J., Ko, J., Leinenweber, K., Liu, X., Li, B., Meng, Y., Pacalo, R.E.G., Vaughan, M.T., Wang, Y., Yeganeh-Haeri, A., 1994. Perovskite at high P–T conditions: an in situ synchrotron X ray diffraction study of NaMgF₃ perovskite. *J. Geophys. Res.* 99 (B2), 2871–2885.